Elasticity, Plasticity and Fracture Toughness of REBCO Coated Conductors Characterized via Micromechanical Tests at Room Temperature

G. Vernassa, M. Rusinowicz, S. Kalácska, S. Sao-Joao, L. Bottura, H. Felice, B. Bordini, J.-M. Bergheau, and G. Kermouche

***Abstract*—REBCO, the leading candidate conductor for ultra high field magnets, is typically produced in the form of thin tapes, consisting of multiple layers of diverse materials with very different natures and properties. Knowledge of the mechanical properties of these different layers is crucial for magnet design. In this paper, we propose a methodology to measure the elasticity, plasticity and fracture toughness of conductor layer materials, at the scale of its constituents, based on nanoindentation, micropillar compression and micropillar splitting techniques. Measurements with these techniques are carried out at room temperature on a commercial conductor, and the results obtained are compared to the values found in the literature and to those specified by the manufacturers.**

***Index Terms*—High-temperature superconductors (HTS), Mechanical properties, Micromechanical testing, REBCO.**

I. Introduction

Rare-Earth Barium Copper Oxide (REBCO) Coated Conductors (CC) are currently the most promising candidates for manufacturing Ultra High Field (UHF) superconducting magnets [1], [2]. This family of High Temperature Superconductors (HTS) is characterized by high mechanical strength under certain loading orientations [3] and a large electrodynamic stability margin [4], in addition to their high critical temperature ($T_c \sim 90$ K) and high engineering critical current densities (I_c/width ~ 1150 A cm$^{-}1$, at 4.2 K and 19 T parallel field [5]). Recently, REBCO CCs have received large attention for the potential use in coils for compact thermonuclear fusion reactors [6]. This spurred the interest of researchers to look for potential applications of REBCO CC in several other fields such as nuclear magnetic resonance (NMR) magnets [7], HTS motors [8] and cryocooled magnets [9] to name a few. This, has also been accelerated by the recent record field of 45.5 T achieved by the national high magnetic field laboratory (NHMFL) [11] with a 14.4 T REBCO insert coil inside a 31.1 T background resistive solenoid. Mechanical calculations estimated that the coil operated at an average hoop stress level of ~ 1 GPa [12], and peak stress levels as high as 1420 MPa, when considering the effects of screening currents-induced stresses (SCIS) [12]. These high stresses are also expected in a 40-60 T solenoid [13] which is under study at CERN, the European Organization for Nuclear Research, in the context of the technological demonstrators for a future Muon Collider [14], which is where our work finds its context .

For a reliable and detailed design of such systems, accurate knowledge of the mechanical properties of the materials is of paramount importance. However, the complex structure of REBCO CCs, consisting of multiple layers with thicknesses ranging from 1 to 100 μm, makes it impractical or infeasible to characterize each layer independently. As a result, researchers have frequently relied on well-established macroscopic testing methods, adapted to REBCO tapes to inversely determine the mechanical properties of the individual layers [15]. Other approaches within the community include macroscopic measurements on bulk materials, such as the three-point bending test described in [16] or the fracture toughness characterization of REBCO bulks [17]. However, these methodologies are difficult to scale to REBCO CCs due to the size effects peculiar to ceramics [18]. To our knowledge, up to date, the only published mechanical measurements of REBCO's properties at the microscale are those reported in [18], where researchers have characterized the elastic properties and fracture toughness of a GdBCO layer via the microcantilever beam method coupled with a dedicated Finite Element model. This methodology however has never been adopted on other REBCO CCs, and the results of [18] remain an isolated case of application on a specific tape. Given the large variety of architectures commercially available and the importance of the mechanical properties of these materials, we propose the application of small scale mechanical testing to determine the properties of REBCO CCs by performing nano/micromechanical experiments that can be applied directly to the REBCO tape layers. In this paper, we report on our first measurements based on instrumented nanoindentation, micropillar compression and splitting tests conducted on a commercial REBCO CC. Although the end goal is the application of these methodologies at cryogenic temperatures, in this campaign we only focused on deploying them at room temperature. We therefore describe the techniques, discuss the results in terms of elastic, plastic, and fracture properties, and finally compare the obtained values to those available in the literature where applicable.

G. Vernassa is with CERN, CH-1211 Geneva, Switzerland and the École des Mines Saint-Etienne, CNRS, UMR5307 LGF, Centre SMS, 42023 Saint Etienne, France.

M. Rusinowicz, S. Kalácska, S. Sao-Joao, and G. Kermouche are with the École des Mines Saint-Etienne, CNRS, UMR5307 LGF, Centre SMS, 42023 Saint Etienne, France.

L. Bottura, and B. Bordini are with CERN, CH-1211 Geneva, Switzerland.

J.-M. Bergheau is with the Univ Lyon, École Centrale Lyon, CNRS, ENTPE, LTDS, UMR5513, ENISE, F-42023 Saint-Étienne, France.

H. Felice is with the CEA-Saclay, IRFU, Univ. Paris Saclay, F-91191 Gif Sur Yvette, France.

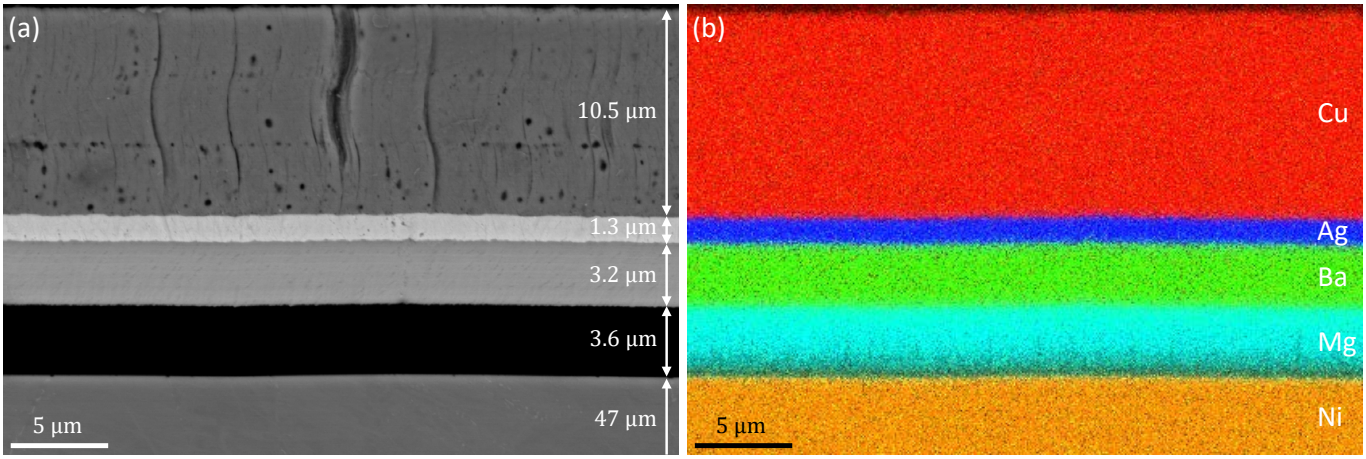

Fig. 1. (a) SEM image of the multilayer stack in a cross-section of the REBCO tape showing, from bottom to top: Hastelloy substrate, MgO buffer layer, REBCO layer, silver layer, and copper layer. (b) EDS chemical analysis verifying the nature of the layers by the presence of their major constituent element.

II. Materials and Methods

A. REBCO tape preparation

In this work, the individual layers of a commercial tape from the manufacturer THEVA were studied. These layers consist of a 47 µm thick Hastelloy substrate, a 3.6 µm thick magnesium oxide (MgO) buffer layer, a 3.2 µm thick REBCO (YBCO) layer, a 1.3 µm thick silver (Ag) layer, and a 10.5 µm thick copper (Cu) layer. Fig. 1(a) presents a cross-sectional SEM (scanning electron microscopy) image of the tape, and Fig. 1(b) shows the EDX (energy-dispersive X-ray spectroscopy) chemical analysis performed on this cross-section to clearly identify the layers through their major constituent element.

All nano/micromechanical tests were performed on the individual layers of the tape in cross-section, which was cut with scissors, embedded in cold resin (Buehler EpoThin™ 2 epoxy resin with hardener) to prevent delamination of the layers, and mechanically polished with silicon carbide papers of progressively small particle size, to a finish with colloidal silica of particle size 0.03 µm. The surface layer affected by polishing is expected to be of the same order of magnitude as the finishing particle size, i.e. a few tens of nanometers, meaning that our measurements are not impacted by it since they concern much greater depths, ranging between 150 nm to 1500 nm as it will be seen later. Micropillars were then machined perpendicularly to the cross-sectional cut, i.e. parallel to the surface of the substrate, by focused ion beam (FIB) milling using a FEI Helios NanoLab DualBeam 600i SEM. Initially, high current conditions (30 kV, 2.5 nA) were applied to achieve the overall shape of the pillar, followed by gradually reducing the current down to 80 pA to obtain the final geometry. The dimensions of the pillars measured by SEM are summarized in Table I.

TABLE I
Top diameter d_{top}, bottom diameter d_{bot}, average radius r_{avg} and height h_{pil} of the pillars machined in the different materials for compression (C) and splitting (S) tests.

	Hastelloy (C)	Copper (C)	REBCO (C)	REBCO (S)
d_{top} (µm)	~ 3.3	~ 2.6	~ 2.0	~ 2.0
d_{bot} (µm)	~ 3.9	~ 3.0	~ 2.4	~ 2.4
r_{avg} (µm)	~ 1.8	~ 1.4	~ 1.1	~ 1.1
h_{pil} (µm)	~ 5.0	~ 4.0	~ 5.5	~ 3.0

B. Instrumented nanoindentation

Instrumented nanoindentation involves applying a normal load to a very hard and stiff tip while measuring the penetration depth of the tip during the loading (indentation) and unloading (retraction) phases. By monitoring the penetration depth h, the load F and the contact stiffness S defined as the slope of the $F-h$ curve at the early stage of unloading, the elastic modulus E and hardness H of the material can be measured.

Nanoindentation tests were performed using the load-controlled DCM (dynamic contact module) head of a MTS XP nanoindenter. A diamond Berkovich tip was used, with its geometry calibrated on a fused silica reference sample following the Oliver and Pharr method [19] to obtain the area function relating the projected contact area A_{c} to the contact depth h_{c}. The tests were conducted with a targeted loading rate of $\dot{F}/F = 0.05\,\mathrm{s}^{-1}$ (indentation strain rate $\dot{h}/h \approx 0.025\,\mathrm{s}^{-1}$) up to a maximum load of 15 mN. The continuous stiffness measurement (CSM) mode was employed to measure the contact stiffness as a function of penetration depth, allowing continuous extraction of the elastic modulus and hardness during indentation. A matrix of 49 indents was made in the relatively thick Hastelloy substrate, while individual indents were targeted in the much thinner layers, using a $40\times$ optical objective, resulting in a total of $5-10$ indents per layer for Cu, MgO and REBCO. Fig. 2(a) shows an optical microscopy overview of the residual indentation imprints in the different layers, and Fig. 2(b)-(c) show SEM images of some representative imprints. The mechanical properties presented hereafter were extracted at a depth of 150 nm to strike a balance between minimizing tip defect effect at shallow depths and limiting the composite effect of surrounding layers at greater depths.

In terms of post-processing, the elastic modulus E and

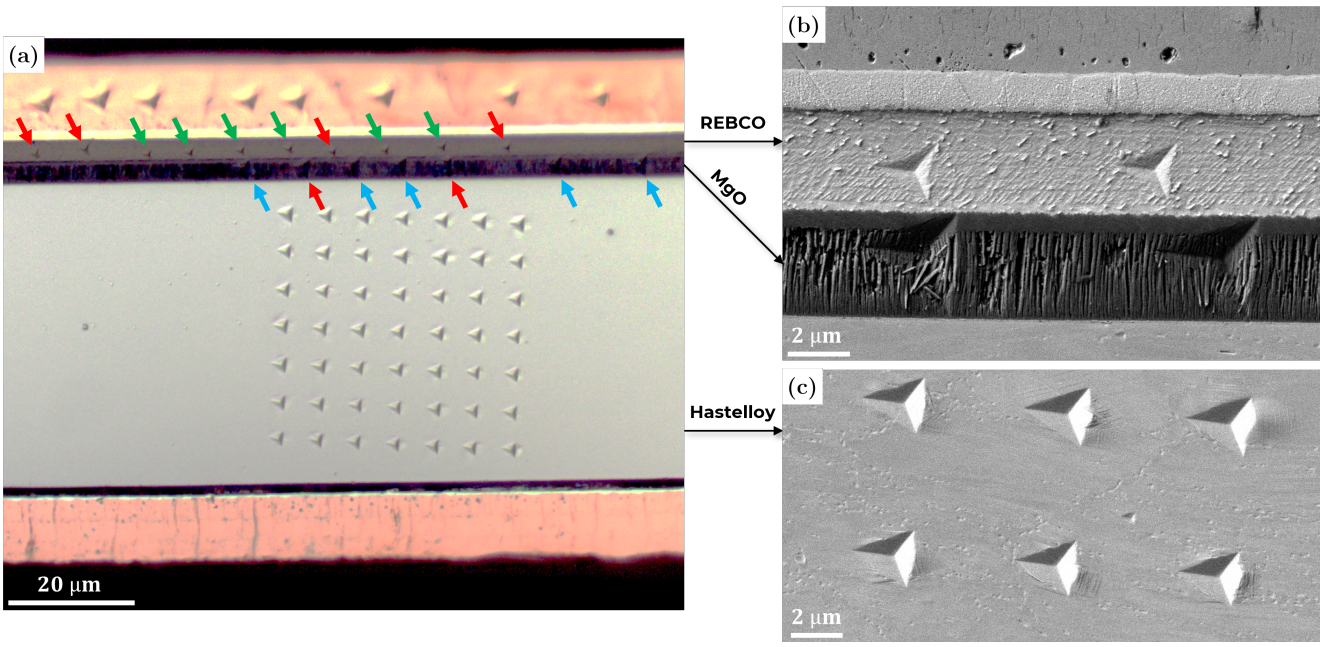

Fig. 2. (a) Optical image of the residual indentation imprints in the Hastelloy, copper, MgO (blue arrows) and REBCO (green arrows) layers. Red arrows indicate tests rejected due to being too close to other layers because of poor targeting. (b) SEM images of the residual indentation imprints in the REBCO and MgO layers. (c) SEM images of the residual indentation imprints in the Hastelloy layer.

hardness H of the materials were determined using Sneddon's equation and Meyer's definition, respectively:

$$E^* = \frac{\sqrt{\pi}}{2}\frac{S}{\sqrt{A_c}} \quad , \quad \frac{1}{E^*} = \frac{1-\nu_t^2}{E_t} + \frac{1-\nu^2}{E} \tag{1}$$

$$H = \frac{F}{A_c} \tag{2}$$

with E^* the reduced elastic modulus, $E_t = 1141\,\text{GPa}$ and $\nu_t = 0.07$ the elastic modulus and Poisson's ratio of the diamond tip, ν the Poisson's ratio of the tested material, and A_c the projected contact area between the tip surface and the sample surface. Given the very different natures of the materials in the multilayer stack (ductile metals, brittle ceramics), the contact area was estimated using Loubet's model [20], which captures both sink-in and pile-up rheologies:

$$h_c = 1.2\left(h - \frac{F}{S}\right) \tag{3}$$

with h_c the contact depth, converted to contact area through the tip area function.

To compare nanoindentation tests to more common uniaxial tensile tests of REBCO tapes found in the literature, hardness was converted into a representative stress σ_r corresponding to the flow stress associated with $\sim 8\,\%$ plastic strain. Kermouche's definition [21] was used for a Berkovich tip:

$$\sigma_r = \frac{0.085H}{0.235 - 0.784\dfrac{H}{E}} \tag{4}$$

C. Micropillar compression

Micropillar compression involves applying a displacement to a flat punch while measuring the load response of the sample. By monitoring the displacement of the punch u and the load F, the whole stress-train curve can be extracted directly within one test [22].

Microcompression tests were conducted using an *in situ* displacement-controlled Alemnis ASA nanoindenter installed in a Zeiss Gemini Supra 55VP SEM to target and visualize the pillars. A 5 µm diameter diamond flat punch was used. The tests were performed at a displacement speed of 100 nm/s up to a maximum displacement of approximately one-third of the initial pillar height. To obtain the true displacement of the pillar u_{pil}, the punch displacement u was corrected by subtracting the contributions of the frame stiffness S_f ($= 1100\,\text{mN/µm}$ determined by a calibration procedure) and the substrate stiffness S_s ($= 2E^* r_{avg}$ estimated by Sneddon's equation, where E^* is the reduced elastic modulus of the material measured by nanoindentation and r_{avg} is the initial average radius of the pillar):

$$u_{pil} = u - \frac{F}{S_{eff}} \quad , \quad \frac{1}{S_{eff}} = \frac{1}{S_f} + \frac{1}{S_s} \tag{5}$$

The $F - u_{pil}$ curves were then converted into $\sigma_{true} - \varepsilon_{true}$ curves (true stress-strain) as follows:

$$\varepsilon_{true} = -\ln\left(\frac{h_{pil} - u_{pil}}{h_{pil}}\right) \tag{6}$$

$$\sigma_{true} = \frac{F}{A} \tag{7}$$

where A is the current cross-sectional area of the pillar, determined based on the radial expansion of the pillar [22] with a constant Poisson's ratio of 0.3.

D. Micropillar splitting

Micropillar splitting involves driving a sharp tip into the pillar until it fractures. The critical load F_c at which the pillar splits for the first time allows the determination of the fracture toughness of the material using the following relation [23]:

$$K_c = \gamma \frac{F_c}{r_{avg}^{3/2}} \quad (8)$$

where γ is a coefficient that depends on the elastic-plastic properties of the material (E/H ratio) and the geometry of the indenter. Splitting tests on the REBCO were conducted with the same *in situ* setup used for compression, but with a cube corner tip and a displacement rate of 20 nm/s. The γ coefficient was estimated to be 0.76 based on the properties of REBCO obtained through nanoindentation and the geometry of the tip used [23].

III. Results and Discussions

A. Elastic-plastic properties of individual layers measured by instrumented nanoindentation

Table II reports the elastic-plastic properties of Hastelloy, Cu, MgO and REBCO layers obtained by nanoindentation. Focusing on the elastic modulus, we observe that the values measured for Hastelloy fall within the range commonly reported in the literature and on manufacturers' data sheets [24], differing by only a few percentage points. Interestingly, the measured elastic modulus for the electroplated copper is relatively at the lower end of the expected range of 80 to 110 GPa. However, similar values have been reported by Ilin et al. [15] where the properties of electroplated copper were indirectly identified from tensile tests on SuperPower® tapes, yielding an elastic modulus of $E = 80$ GPa at room temperature.

These results encouraged the application of this methodology to the REBCO and MgO layers, for which little or no data are currently available in the literature. Indeed, to the best of our knowledge, the elastic properties of REBCO have only been measured on single crystal bulks using methods such as the three-point bending test [16], nano or Vickers indentation [25]–[27], or even techniques based on phonon dispersion curves [28]. For REBCO, reported values range from 149 to 185 GPa, obtained through Vickers indentation, as cited in [26] and [27].

Our measured value for REBCO is $E = 155$ GPa, which falls in the aforementioned range, and it is also remarkably close to the value of 157 GPa [29], often used as reference value by magnet designers. Regarding the MgO layer, we measured an elastic modulus of $E = 95$ GPa, which, to our knowledge, is the first publicly reported measurement for this material.

TABLE II
Mechanical properties of REBCO tape layers measured by nanoindentation at 150 nm depth (elastic modulus E, hardness H, representative stress σ_r) and micropillar splitting (fracture toughness K_c).

	Hastelloy	Copper	MgO	REBCO
E (GPa)	197 ± 5	84 ± 3	95 ± 4	155 ± 5
H (GPa)	4.80 ± 0.17	1.55 ± 0.10	2.28 ± 0.15	8.90 ± 0.47
σ_r (GPa)	1.90 ± 0.06	0.60 ± 0.04	0.90 ± 0.06	4.00 ± 0.19
K_c (MPa·m$^{1/2}$)	-	-	-	1.34 ± 0.12

B. Plastic flow behavior of metal layers measured by micropillar compression

The true stress-strain curves of Hastelloy and copper layers obtained by micropillar compression are presented in Fig. 3(a). For Hastelloy, the initial yield strength at which the material begins to exhibit plasticity ranges from 1.2 to 1.4 GPa. These values are at the upper end of the range of yield stresses measured in tensile tests on samples extracted from REBCO tapes [15], [30], with measured $R_{p0.2}$ values at room temperature of 891 MPa and 1225 MPa respectively, but are in good

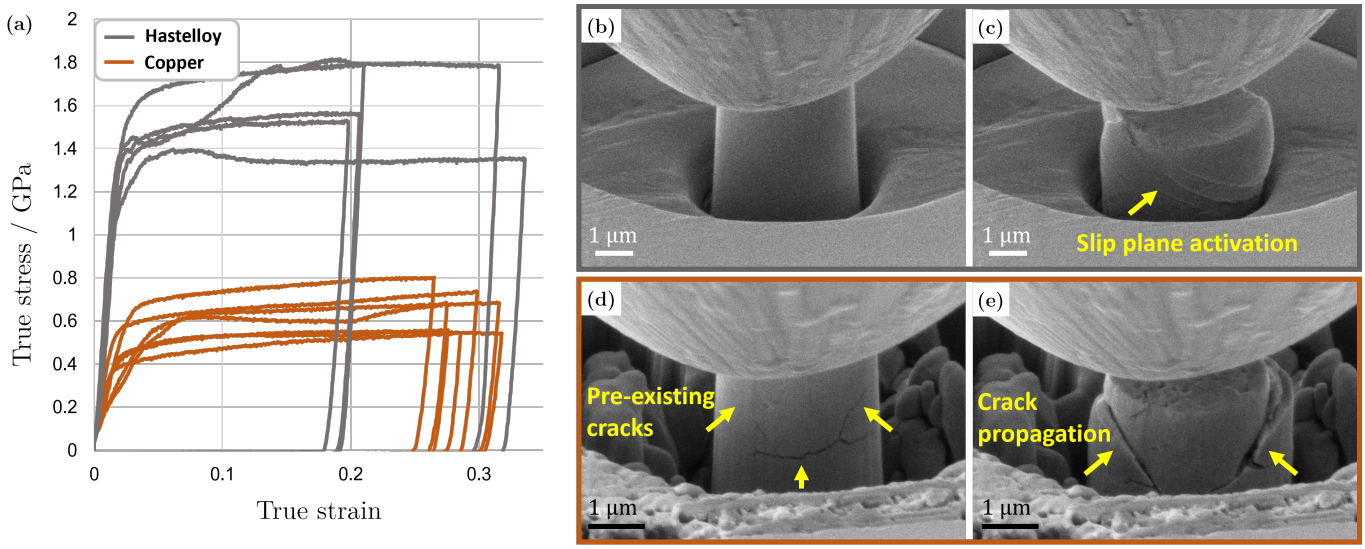

Fig. 3. (a) True stress-strain curves of Hastelloy and copper layers obtained by micropillar compression. (b)-(c) SEM images of a representative Hastelloy pillar before and after compression, respectively. (d)-(e) SEM images of a representative copper pillar before and after compression, respectively.

agreement with those measured on bare substrates, as reported by [31]. Indeed, Radcliff et al. showed that yield strength of the substrate is affected by the heat cycle it sees during the REBCO deposition process, decreasing from 1.5 to 1.2 GPa, as the process temperature increases from 700 to 800 °C. This suggests that the manufacturing processes adopted by different manufacturers can significantly influence the yield strength of the substrate material, leading to some variation in the measured values depending on the manufacturer.

In the plastic flow regime, we can observe a substantial scattering between the curves, though the stress levels saturate in most cases between 1.5 and 1.8 GPa, slightly lower than the representative stress of 1.9 GPa obtained by nanoindentation. Regarding copper, the curves are also scattered, but the level of plastic flow is clearly lower than that of Hastelloy, with little strain-hardening and a flow stress saturating at $\sim$ 0.6 GPa on average. This value perfectly matches the representative stress of 0.6 GPa obtained by nanoindentation and is also in agreement with other micropillar compression studies on physical vapor deposited (PVD) copper for microelectronic applications [32].

To better understand the origin of the scatter in the experimental stress-strain curves as well as to unravel the plastic deformation mechanisms in each material, Fig. 3(b)-(c) and Fig. 3(d)-(e) show SEM images of representative Hastelloy and copper pillars, respectively, before and after compression.

Before compression, the Hastelloy pillar exhibits no visible defects, while after compression, the pillar is sheared along well-defined planes. These planes are in fact slip planes activated during mechanical loading. It is important to note that Hastelloy grains have a size of 5-10 µm, larger than the pillar size, meaning we are essentially compressing a single crystal. The activation of certain slip systems rather than others depends on the crystal orientation relative to the loading direction. This explains why the stress-strain curves of Hastelloy are scattered based on the grain orientation in which the pillar was machined. It also explains why nanoindentation gives a higher flow stress value compared to compression, as the multiaxial stress state generated by the pyramidal tip penetration activates multiple slip systems, which mutually hinder each other and overall harden the material.

The copper pillar, on the contrary, has many defects in its initial microstructure, particularly porosities (cf. Fig. 1(a)) and cracks (cf. Fig. 3(d)). These defects are stress concentration sites that drive the plastic deformation process, as observed in Fig. 3(e) where the top of the pillar has collapsed along the path of pre-existing conical cracks. The scatter in the copper stress-strain curves is thus explained by the statistical presence of defects in each pillar.

C. Fracture toughness of REBCO layer measured by micropillar splitting

The true stress-strain curve of a representative compression test of a REBCO micropillar is shown in Fig. 4(a), with SEM images of the pillar before compression and after the first fracture in Fig. 4(b)-(c). It is observed from the stress-strain curve that the stress level increases almost proportionally with the strain level up to a stress of $\sim$ 2.5 GPa (strain of $\sim$ 2 %), where the stress drops abruptly. This stress drop is due to the fracture of the pillar by buckling, as evidenced

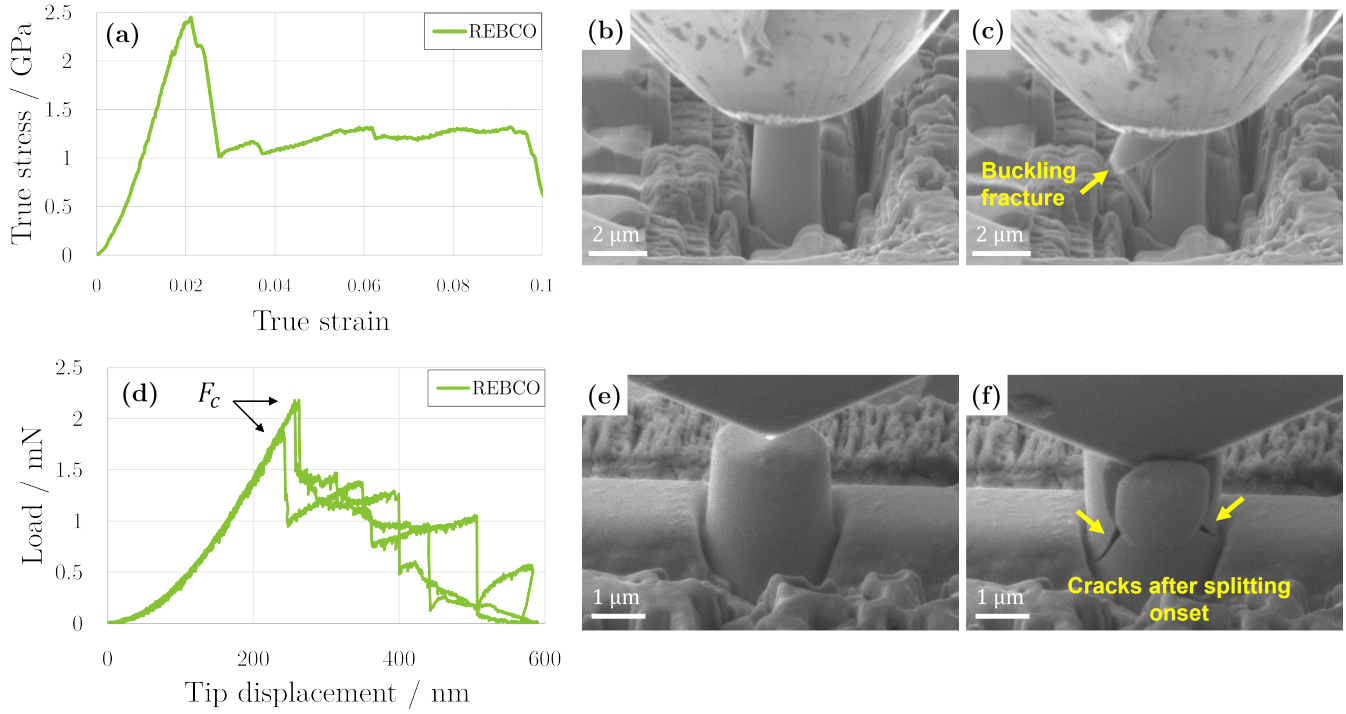

Fig. 4. (a) True stress-strain curve obtained by compression of a REBCO micropillar. (b)-(c) SEM images of the REBCO pillar before compression and after the first fracture, respectively. (d) Load-displacement curves obtained from splitting REBCO micropillars. (e)-(f) SEM images of a representative REBCO pillar before splitting and after the first fracture, respectively.

by Fig. 4(c), a typical failure mode for brittle materials as previously shown with the compression of carbon fiber pillars [33]. Thus, REBCO appears to behave like a brittle material. The stress level at which fracture occurs confirms this, since the fracture stress of 2.5 GPa obtained by microcompression is lower than the plastic flow stress of 4 GPa measured by nanoindentation. REBCO is therefore brittle in the sense that it fractures within its elastic domain. The fracture toughness of REBCO was determined by micropillar splitting, which is particularly well-suited for brittle materials.

The load-displacement curves obtained from splitting three REBCO micropillars are shown in Fig. 4(d), with SEM images of a representative pillar before splitting and after the first fracture in Fig. 4(e)-(f). The loading curves are very reproducible and lead to a critical load of around 2 mN at which the pillar splits instantly, as observed in Fig. 4(f), giving the fracture toughness of REBCO at $1.34 \pm 0.12\,\mathrm{MPa.m}^{1/2}$ (value reported in Table II). This value is very close to that measured on another type of REBCO using microcantilever beam bending, which range between 0.8 and $1.8\,\mathrm{MPa{\cdot}m}^{1/2}$ [18]. However, micropillar splitting is an easier and more robust method as it does not depend on the geometry of a notch, which is particularly difficult to machine, resulting in very low dispersion in fracture toughness values.

IV. Conclusion

The accurate knowledge of the elastic-plastic and fracture toughness properties of REBCO CC layers' materials is a fundamental requirement for the faithful stress analyses of superconducting magnet systems. This work demonstrates how the combination of three standard micromechanical experiments can effectively quantify intrinsic mechanical properties at the constituent scale of superconducting tape layers. Nanoindentation proves efficient for measuring the elastic modulus and yield stress. Micropillar testing provides valuable insights into plastic flow behavior and enables the quantification of stress-strain curves. Micropillar splitting is a promising test for assessing fracture toughness, especially on brittle materials such as the REBCO layer investigated in this paper. The results obtained in this campaign show excellent agreement with literature data. Thanks to its versatility, the utilized methodology can be applied to any architecture of technical superconductors, both Low Temperature Superconductors (LTS) and High Temperature Superconductors (HTS). Although the micromechanical tests in this study were conducted at room temperature, recent advances in cryogenic micromechanical testing suggest that this methodology may soon be adaptable to temperatures closer to real operational conditions.

References

[1] Y. H. Zhou, D. Park and Y. Iwasa, "Review of progress and challenges of key mechanical issues in high-field superconducting magnets", *National Science Review*, vol. 10, pp. nwad001, 2023.

[2] C. Senatore, M. Alessandrini, A. Lucarelli, R. Tediosi, D. Uglietti and Y. Iwasa, "Progresses and challenges in the development of high-field solenoidal magnets based on RE123 coated conductors", *Superconductor Science and Technology*, vol. 27, pp. 103001, 2014.

[3] C. Barth and G. Mondonico and C. Senatore. "Electro-mechanical properties of REBCO coated conductors from various industrial manufacturers at 77 K, self-field and 4.2 K, 19 T", *Superconductor Science and Technology*, vol. 28, 4 2015.

[4] R. Grabovickic, J. W. Lue, M. J. Gouge, J. A. Demko and R. C. Duckworth, "Measurements of temperature dependence of the stability and quench propagation of a 20-cm-long RABiTS Y-Ba-Cu-O tape", *IEEE Transactions on Applied Superconductivity*, vol. 13, pp. 1726–1730, 2003.

[5] C. Senatore, M. Bonura and T. Bagni, "REBCO tapes for applications in ultra-high fields: critical current surface and scaling relations" *Superconductor Science and Technology*, vol. 37, 2024, 115013.

[6] L. Bottura, "Collider magnets (incl. muon collider)", *CAS course on "Normal- and Superconducting Magnets"*, 2023, St. Pölten, Austria.

[7] D. Park, J. Bascuñán, Y. Li, W. Lee, Y. Choi, Y. Iwasa, "Design Overview of the MIT 1.3-GHz LTS/HTS NMR Magnet with a New REBCO Insert", *IEEE Trans Appl Supercond.*, Aug 2021; Vol. 31, DOI: 10.1109/tasc.2021.3064006.

[8] P. Alvarez, M. Satrústegui, S. G. Scheifler, J. Bastarrarena, L. G. López, M. Martinez-Iturralde, "Design of a HTS 2 MW Electric Motor for Single-Aisle Regional Aircraft", in *IEEE Access*, vol. 11, pp. 144325-144336, 2023, doi: 10.1109/ACCESS.2023.3343816.

[9] K. Watanabe, S. Awaji, G. Nishijima et al., "Cryogen-Free 23 T Superconducting Magnet Employing an YBa2Cu3O7 Coated Conductor Insert" *J. Supercond. Nov. Magn.*, Vol. 24, 993–997, 2011.

[10] S. Yoon, J. Kim, H. Lee, S. Hahn and S. H. Moon "26 T 35 mm all-GdBa2Cu3O7-x multi-width no-insulation superconducting magnet", *Superconductor Science and Technology*, vol. 29, pp. 04LT04, 2016.

[11] S. Hahn, K. Kim, K. Kim, X. Hu, T. Painter, I. Dixon, S. Kim, K. R. Bhattarai, S. Noguchi, J. Jaroszynski and D. C. Larbalestier, "45.5-tesla direct-current magnetic field generated with a high-temperature superconducting magnet", *Nature*, vol. 570, pp. 496–499, 2019.

[12] X. Hu, M. Small, K. Kim, K. Kim, K. Bhattarai, A. Polyanskii, K. Radcliff, J. Jaroszynski, U. Bong, J. H. Park, S. Hahn and D. Larbalestier, "Analyses of the plastic deformation of coated conductors deconstructed from ultra-high field test coils", *Superconductor Science and Technology*, vol. 33, pp. 095012, 2020.

[13] B. Bordini, C. Accettura, A. Bertarelli, L. Bottura, A. Dudarev, A. Kolehmainen, T. Mulder, A. Verweij and M. Wozniak, "Conceptual Design of a ReBCO Non/Metal-Insulated Ultra-High Field Solenoid for the Muon Collider", *IEEE Transactions on Applied Superconductivity*, vol. 34, pp. 1–10, 2024.

[14] L. Bottura and D. Aguglia and B. Auchmann and T. Arndt and J. Beard and A. Bersani and F. Boattini and M. Breschi and B. Caiffi and X. Chaud and M. Dam and F. Debray and H. De Gersem and E. De Matteis and A. Dudarev and S. Farinon and A. Kario and R. Losito and S. Mariotto and M. Mentink and R. Musenich and T. Ogitsu and M. Prioli and L. Quettier and L. Rossi and D. Schulte and C. Senatore and M. Sorbi and M. Statera and H. Ten Kate and R. U. Valente and A. Yamamoto and Y. Yang, "A Work Proposal for a Collaborative Study of Magnet Technology for a Future Muon Collider", In *Snowmass 2021*, 3 2022, arXiv:2203.13998 [physics.acc-ph] http://arxiv.org/abs/2203.13998,

[15] K. Ilin, K. A. Yagotintsev, C. Zhou, P. Gao, J. Kosse, S. J. Otten, W. A. Wessel, T. J. Haugan, D. C. V. D. Laan and A. Nijhuis, "Experiments and FE modeling of stress-strain state in ReBCO tape under tensile, torsional and transverse load", *Superconductor Science and Technology*, vol. 28, pp. 055006, 2015.

[16] T. Okudera, A. Murakami, K. Katagiri, K. Kasaba, Y. Shoji, K. Noto, N. Sakai and M. Murakami,, "Fracture toughness evaluation of YBCO bulk superconductor", *Physica C: Superconductivity and its applications*, vol. 392-396, pp. 628–633, 2003.

[17] K. Konstantopoulou, "Mechanical Behavior of 2G REBCO HTS at 77 and 300 K", *Thesis (Doctoral)*, 2015.

[18] S. Muto, W. Hirata, S. Fujita, K. Akashi, Y. Iijima and M. Daibo, "Micromechanical Property Evaluation Of REBCO Coated Conductors Using Microcantilever Beam Method", *IEEE Transactions on Applied Superconductivity*, vol. 30, pp. 8400904, 2020.

[19] W. C. Oliver and G. M. Pharr, "An improved technique for determining hardness and elastic modulus using load and displacement sensing indentation experiments", *Journal of Materials Research*, vol. 7, pp. 1564–1583, 1992.

[20] J. L. Loubet, M. Bauer, A. Tonck, S. Bec and B. Gauthier-Manue, "Nanoindentation with a Surface Force Apparatus", *Mechanical Properties and Deformation Behavior of Materials Having Ultra-Fine Microstructures.*, NATO ASI Series, vol. 233. Springer, Dordrecht, pp. 429–447, 1993.

[21] G. Kermouche, J. L. Loubet and J. M. Bergheau, "Extraction of stress-strain curves of elastic-viscoplastic solids using conical/pyramidal indentation testing with application to polymers", *Mechanics of Materials*, vol. 40, pp. 271–283, 2008.

[22] G. Kermouche, G. Guillonneau, J. Michler, J. Teisseire and E. Barthel, "Perfectly plastic flow in silica glass", *Acta Materialia*, vol. 114, pp. 146–153, 2016.

[23] M. Ghidelli, M. Sebastiani, K. E. Johanns and G. M. Pharr, "Effects of indenter angle on micro-scale fracture toughness measurement by pillar splitting", *Journal of the American Ceramic Society*, vol. 100, pp. 5731–5738, 2017.

[24] MatWeb, "Online Materials Information Resource", [Online], https://www.matweb.com/index.aspx, Accessed: 2024-08-22.

[25] J. J. Roa, E. Jiménez-Piqué, X. G. Capdevila and M. Segarra, "Nanoindentation with spherical tips of single crystals of YBCO textured by the Bridgman technique: Determination of indentation stress–strain curves", *Journal of the European Ceramic Society*, vol. 30, pp. 1477–1482, 2010.

[26] C. E. Foerster, E. Lima, P. R. Jr., F. C. Serbena, C. M. Lepienski, M. P. Cantao, A. R. Jurelo and X. Obradors, "Mechanical properties of Ag-doped top-seeded melt-grown YBCO pellets", *Brazilian Journal of Physics*, vol. 38, pp. 341–345, 2008.

[27] Y. Yoshino, A. Iwabuchi, K. Noto, N. Sakai and M. Murakami, "Vickers hardness properties of YBCO bulk superconductor at cryogenic temperatures", *Physica C: Superconductivity*, vol. 357-360, pp. 796–798, 2001.

[28] W. Reichardt, L. Pintschovius, B. Hennion and F. Collin, "Inelastic neutron scattering study of YBa2Cu3O7-x", *Superconductor Science and Technology*, vol. 1, pp. 173–176, 1988.

[29] A. S. Raynes, S. W. Freiman, F. W. Gayle and D. L. Kaiser, "Fracture toughness of YBa2Cu3O6+δ single crystals: Anisotropy and twinning effects", *Journal of Applied Physics*, vol. 70, pp. 5254–5257, 1991.

[30] Y. Zhang, D. W. Hazelton, R. Kelley, M. Kasahara, R. Nakasaki, H. Sakamoto, and A. Polyanskii, "Stress-Strain Relationship, Critical Strain (Stress) and Irreversible Strain (Stress) of IBAD-MOCVD-Based 2G HTS Wires under Uniaxial Tension", *IEEE Transactions on Applied Superconductivity*, vol. 26, pp. 1–6, 2016.

[31] K. J. Radcliff, R. P. Walsh, D. C. Larbalestier, and S. Hahn, "The Effect of Reinforcement Substrate Alloy Selection on Mechanical Properties of REBCO Coated Conductors", *IOP Conference Series: Materials Science and Engineering*, vol. 756, pp. 012023, 2020.

[32] I. Malkorra, S. Sao-Joao, U. Costa, D. Chalavoux, S. Bucher, N. Perardel and G. Kermouche, "Multi-scale in-situ micro-mechanical characterization of Polymer Core Solder Ball (PCSB) coatings for BGA interconnections", *Microelectronics Reliability*, vol. 148, pp. 115135, 2023.

[33] T. S. Guruprasad, V. Keryvin, G. Kermouche, Y. Marthouret and S. Sao-Joao, "Compressive behaviour of carbon fibres micropillars by in situ SEM nanocompression", *Composites Part A*, vol. 173, pp. 107699, 2023.